

Stationary Ca^{2+} nanodomains in the presence of buffers with two binding sites

Running title: Ca^{2+} nanodomains for 2:1 Ca^{2+} buffers

Yinbo Chen and Victor Matveev

Department of Mathematical Sciences, New Jersey Institute of Technology, NJ, USA

ABSTRACT

We examine closed-form approximations for the equilibrium Ca^{2+} and buffer concentrations near a point Ca^{2+} source representing a Ca^{2+} channel, in the presence of a mobile buffer with two Ca^{2+} binding sites activated sequentially and possessing distinct binding affinities and kinetics. This allows to model the impact on Ca^{2+} nanodomains of realistic endogenous Ca^{2+} buffers characterized by cooperative Ca^{2+} binding, such as calretinin. The approximations we present involve a combination of rational and exponential functions, whose parameters are constrained using the series interpolation method that we recently introduced for the case of simpler Ca^{2+} buffers with a single Ca^{2+} binding site. We conduct extensive parameter sensitivity analysis and show that the obtained closed-form approximations achieve reasonable qualitative accuracy for a wide range of buffer's Ca^{2+} binding properties and other relevant model parameters. In particular, the accuracy of the newly derived approximants exceeds that of the Rapid Buffering approximation in large portions of the relevant parameter space.

STATEMENT OF SIGNIFICANCE

Closed-form approximations describing equilibrium distribution of Ca^{2+} in the vicinity of an open Ca^{2+} channel proved useful for the modeling of local Ca^{2+} signals underlying secretory vesicle exocytosis, muscle contraction and other cell processes. Such approximations provide an efficient method for estimating Ca^{2+} and buffer concentrations without computationally expensive numerical simulations. However, while most biological buffers have multiple Ca^{2+} binding sites, much of prior modeling work considered Ca^{2+} dynamics in the presence of Ca^{2+} buffers with a single Ca^{2+} binding site. Here we extend such modeling of equilibrium Ca^{2+} nanodomains to the case of Ca^{2+} buffers with two binding sites, allowing to gain deeper insight into the impact of more realistic Ca^{2+} buffers, including cooperative buffers, on cell Ca^{2+} dynamics.

Keywords: calcium nanodomain, calcium buffer, stationary solution, equilibrium approximation, rapid buffering approximation, reaction-diffusion system, calmodulin, calretinin

INTRODUCTION

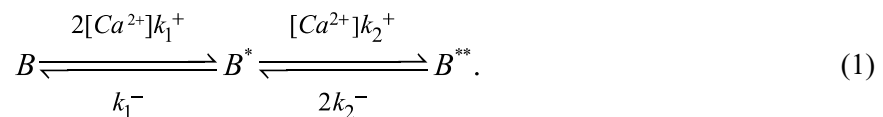
Accurate description of Ca^{2+} concentration ($[\text{Ca}^{2+}]$) elevations formed near open Ca^{2+} channels, termed micro- or nano-domains, is crucial for the understanding of many fundamental cell processes such as synaptic neurotransmitter release, endocrine hormone release, and muscle contraction (1-5). This is particularly true in the case of chemical synaptic transmission, since the fusion (exocytosis) of a presynaptic neurotransmitter-filled vesicle can be triggered by the opening of just a few voltage-gated Ca^{2+} channels (5-10). The characteristic time of synaptic vesicle exocytosis is a fraction of 1 millisecond, while the relevant spatial scale is determined by the Ca^{2+} channel-vesicle separation, on the order of 10-100 nm (4-13). Optical Ca^{2+} imaging is insufficient to track spatio-temporal Ca^{2+} dynamics on such fine temporal and spatial scales, and cannot be carried out without disturbing the Ca^{2+} signal that is being measured. This explains the key role that mathematical and computational modeling has played in the study of vesicle exocytosis, myocyte contraction, and other fundamental processes controlled by localized Ca^{2+} elevations (11-18). The main technical challenge in such modeling stems from the interaction of Ca^{2+} with intracellular Ca^{2+} buffers, which bind most of Ca^{2+} ions upon their entry into the cytoplasm (11, 19). Buffered Ca^{2+} diffusion problem leads to a system of nonlinear partial differential equations, which requires computational modeling. One early insight gained from such computational studies is that $[\text{Ca}^{2+}]$ reaches a quasi-stationary steady state in the vicinity of an open Ca^{2+} channel very quickly, within 10-100 μs , and this quasi-stationary Ca^{2+} nanodomain gradient collapses as quickly after channel closing (14-18). This suggested that equilibrium solutions to the Ca^{2+} reaction-diffusion equations may achieve sufficient accuracy in modeling $[\text{Ca}^{2+}]$ as a function of distance from an open Ca^{2+} channel. Therefore, several closed-form equilibrium Ca^{2+} nanodomain approximations have been developed for the case of buffers with a single Ca^{2+} -binding site, which we will refer to as simple or one-to-one (1:1) Ca^{2+} buffers (11, 20-32). These approximations proved useful in understanding the properties of Ca^{2+} nanodomains and their dependence on the properties of cell Ca^{2+} buffers, and provide a convenient and efficient tool for modeling studies (11, 20-37). More recently, we introduced a new method for approximating Ca^{2+} nanodomains in the presence of 1:1 Ca^{2+} buffers based on matching the short-range and long-range series expansions of the nanodomain $[\text{Ca}^{2+}]$ as a function of distance from the channel, which achieves greater and more uniform accuracy compared to the previous methods in a wide range of relevant model parameters (38, 39). Here we show that this new method, which we refer to as the series interpolation method, can be extended to the case of more complex buffers with two Ca^{2+} binding sites, which we will refer to as 2:1 Ca^{2+} buffers. This allows to accurately model the impact of more realistic Ca^{2+} buffers, all of which have multiple binding sites. For example, many widely expressed Ca^{2+} buffers and sensors such as calretinin and calmodulin contain two EF-hand domains which

cooperatively bind two Ca^{2+} ions, whereby the binding of the second Ca^{2+} ion proceeds with much greater affinity once the first binding site is occupied (40-49).

Among the previously developed approaches, only the Rapid Buffering approximation (RBA) (11, 28-33) has been extended to buffers with two Ca^{2+} -binding sites that we consider in this work (49). However, RBA is based on the assumption that the rate of Ca^{2+} -buffer binding is much faster than the rate of Ca^{2+} diffusion and influx (32), and therefore reactions are at equilibrium throughout the domain. This condition has a complex interplay with the above-mentioned property of cooperative buffers whereby the affinity of the 1st Ca^{2+} binding event is much smaller than that of the 2nd Ca^{2+} binding event. This complex interplay between the two conditions limits the accuracy of the leading-order RBA for realistic Ca^{2+} buffers (49). Finally, other approximations developed for the 1:1 buffering case are based on linearizing the Ca^{2+} -binding reaction (11, 20-26), and therefore are inapplicable to the case of 2:1 Ca^{2+} buffering, which cannot be linearized. Therefore, this work represents the first effort to systematically explore stationary nanodomain approximations in the case of complex 2:1 Ca^{2+} buffers. We perform systematic parameter sensitivity analysis of the newly obtained approximants and demonstrate that they achieve significantly improved approximation accuracy as compared to RBA for a wide range of relevant parameter values, and capture the non-trivial dependence of the bound buffer concentration on the distance from the Ca^{2+} channel.

METHODS

We start with the description of the Ca^{2+} binding and unbinding reactions for buffer molecules with two binding sites (42-49):



Here B , B^* and B^{**} denote respectively the free, partially bound, and fully Ca^{2+} -bound states of the buffer, and $k_{1,2}^+$, $k_{1,2}^-$ are the Ca^{2+} -buffer binding/unbinding rates for each buffer state. Following prior modelling work (32), we will consider a semi-infinite domain bounded by a flat plane representing the cytoplasmic membrane, which contains one or more Ca^{2+} channels. Further, we assume zero flux boundary condition for Ca^{2+} and buffer on the flat plane, so the reflection symmetry allows to extend the domain to infinite space, while doubling the current strength, which places the Ca^{2+} current sources inside the domain (27-30). Denoting free Ca^{2+} concentration as C , and time differentiation as ∂_t , we arrive at the following reaction-diffusion system for the concentrations of all reactants (49):

$$\begin{cases} \partial_t C = D_C \nabla^2 C - R_1 - R_2 + 2 \sum_{k=1}^{N_{Ca}} \sigma_k \delta(\mathbf{r} - \mathbf{r}_k), \\ \partial_t B = D_B \nabla^2 B - R_1, \\ \partial_t B^* = D_B^* \nabla^2 B^* + R_1 - R_2, \\ \partial_t B^{**} = D_B^{**} \nabla^2 B^{**} + R_2, \end{cases} \quad (2)$$

where the reaction terms are given by

$$\begin{cases} R_1 = 2k_1^+ C B - k_1^- B^*, \\ R_2 = k_2^+ C B^* - 2k_2^- B^{**}. \end{cases} \quad (3)$$

In Eq. 2, the point channel-source strengths are $\sigma_k = I_{Ca,k}/(2F)$, where $I_{Ca,k}$ are the amplitudes of individual open Ca^{2+} channels located at positions \mathbf{r}_k , F is the Faraday constant, and N_{Ca} is the number of Ca^{2+} channels. As in the simple-buffer case (30-32, 38, 39, 49-51), there are two conservation laws for the total buffer and the total Ca^{2+} concentrations:

$$\partial_t (B + B^* + B^{**}) = \nabla^2 (D_B B + D_B^* B^* + D_B^{**} B^{**}), \quad (4)$$

$$\begin{aligned} \partial_t (C + B^* + 2B^{**}) &= \nabla^2 (D_C C + D_B^* B^* + 2D_B^{**} B^{**}) \\ &+ 2 \sum_{k=1}^{N_{Ca}} \sigma_k \delta(\mathbf{r} - \mathbf{r}_k). \end{aligned} \quad (5)$$

In this work we focus on equilibrium solutions (see Discussion for the limitations of this approach), which satisfy

$$\begin{cases} D_B \nabla^2 B = R_1, \\ D_B^{**} \nabla^2 B^{**} = -R_2, \\ \nabla^2 (D_B B + D_B^* B^* + D_B^{**} B^{**}) = 0, \\ \nabla^2 (D_C C + D_B^* B^* + 2D_B^{**} B^{**}) = -2 \sum_{k=1}^{N_{Ca}} \sigma_k \delta(\mathbf{r} - \mathbf{r}_k). \end{cases} \quad (6)$$

Here we assume that buffer diffusivity does not change when binding Ca^{2+} ions, $D_B = D_B^* = D_B^{**}$ (this constraint is relaxed in the derivation of RBA in Supporting Material 1). In this case the two conservation laws in Eq. 6 have the following solution (30-32, 38, 39, 49-51):

$$\begin{cases} B + B^* + B^{**} = B_T = const, \\ D_C C + D_B (B^* + 2B^{**}) = \frac{1}{2\pi} \sum_{k=1}^N \frac{\sigma_k}{|\mathbf{r} - \mathbf{r}_k|} + C_T, \end{cases} \quad (7)$$

where constants B_T and C_T are related to the total (bound plus free) buffer and Ca^{2+} concentrations respectively, infinitely far from channel:

$$\begin{cases} B_T = B_\infty + B_\infty^* + B_\infty^{**}, \\ C_T = D_C C_\infty + D_B (B_\infty^* + 2B_\infty^{**}). \end{cases} \quad (8)$$

Here X_∞ denote the concentrations of reactants X infinitely far from the channel, where reactions given by Eq. 3 are at equilibrium. Therefore, all background buffer state concentrations are uniquely determined by the background $[\text{Ca}^{2+}]$, C_∞ , through equilibrium relationships

$$\begin{cases} 2C_\infty B_\infty = K_1 B_\infty^*, \\ C_\infty B_\infty^* = 2K_2 B_\infty^{**}, \end{cases} \quad (9)$$

where $K_{1,2}$ are the affinities of the two reactions in Eqs. 1, 3, given by $K_1 \equiv k_1^- / k_1^+$ and $K_2 \equiv k_2^- / k_2^+$.

We now restrict to the case of a single Ca^{2+} channel of source strength $\sigma = I_{Ca}/(2F)$ at the origin, and look for spherically symmetric solutions, which turns Eq. 6 into a system of ODEs, with the spherically symmetric Laplacian given in terms of the distance from the Ca^{2+} channel, $r=|\mathbf{r}|$: $\nabla^2 = \partial_r^2 + 2\partial_r / r$.

We non-dimensionalize this problem using an approach analogous to the one we used in (38,39,49), which is a slightly modified version of the non-dimensionalization introduced by Smith et al. (32). Namely, we rescale Ca^{2+} and buffer concentrations by the affinity of the 2nd binding step and the background buffer concentration, respectively:

$$c = \frac{C}{K_2}, \quad b = \frac{B}{B_\infty}, \quad b^* = \frac{B^*}{B_\infty}, \quad b^{**} = \frac{B^{**}}{B_\infty}. \quad (10)$$

We also rescale the spatial coordinate ($r/L \rightarrow r$) using the scale parameter that depends on the strength of the Ca^{2+} current,

$$L = \sigma / (2\pi K_2 D_C). \quad (11)$$

This transforms Eqs. 6,7 to the form

$$\begin{cases} \lambda_1 \nabla^2 b = 2\varepsilon cb - b^*, \\ \lambda_2 \nabla^2 b^{**} = -cb^* + 2b^{**}, \\ b + b^* + b^{**} = b_T, \\ c + \frac{V_2}{2} (b^* + 2b^{**}) = \frac{1}{r} + c_T. \end{cases} \quad (12)$$

Here b_T and c_T are the non-dimensional versions of the integration constants given by Eq. 8, related to the total buffer and $[\text{Ca}^{2+}]$ infinitely far from the channel according to (note that $b_\infty=1$ by Eq. 10)

$$\begin{cases} b_T = 1 + b_\infty^* + b_\infty^{**}, \\ c_T = c_\infty + \frac{V_2}{2} (b_\infty^* + 2b_\infty^{**}), \end{cases} \quad (13)$$

with dimensionless parameters

$$\lambda_{1,2} = \frac{D_B}{L^2 k_{1,2}^-}, \quad \nu_{1,2} = \frac{2B_\infty D_B}{K_{1,2} D_C}. \quad (14)$$

Along with c_∞ , parameters $\lambda_{1,2}$ and $\nu_{1,2}$ completely specify the model system. Here $\lambda_{1,2}$ are the dimensionless mobilities of the two buffer states, which depend on buffering kinetics and Ca^{2+} current amplitude through the length scale L (Eq. 11). They quantify the ratio between the rate of diffusion and the rate of Ca^{2+} influx and binding (32). Parameters $\nu_{1,2}$ quantify the overall buffering strength, equal the product of the relative buffer mobility, D_B/D_C , and the two resting buffering capacity parameters, $2B_\infty/K_{1,2}$. For the sake of simplicity, we will also use the following cooperativity parameters, which characterize the difference between the affinities and kinetics of the buffer's two distinct Ca^{2+} -binding sites:

$$\varepsilon = \frac{\nu_1}{\nu_2} = \frac{K_2}{K_1}, \quad \gamma = \frac{\lambda_1}{\lambda_2} = \frac{k_2^-}{k_1^-}. \quad (15)$$

In the case of calretinin and calmodulin, the binding properties have been experimentally estimated (42, 46, 52), and the corresponding values of cooperativity parameters are given in Table 3. These two Ca^{2+} buffers are characterized by highly cooperative Ca^{2+} binding, with $\varepsilon \ll 1$. In the results shown below, we will use the two cooperativity parameters to replace some of the four parameter in Eq. 14. Namely, we will specify our model using either $\{\lambda_2, \nu_2, \varepsilon, \gamma\}$ or $\{\lambda_1, \lambda_2, \varepsilon, q\}$, where $q=1/(1+\nu_1)$ is analogous to the parameter of the same name in the simple buffer case (38, 39).

We now restrict our analysis to the case of zero background $[\text{Ca}^{2+}]$, relegating more general results to Supporting Material 1. With this simplification, we set $c_\infty=c_T=0$ and $b_\infty=b_T=1$ in Eq. 12. Eliminating the Ca^{2+} concentration and the partially-bound buffer concentration variables using the two conservation laws in Eq. 12, we obtain

$$\begin{cases} \lambda_1 \nabla^2 b = 2\varepsilon b \left[\frac{1}{r} - \frac{v_2}{2} (b^{**} - b + 1) \right] + b + b^{**} - 1, \\ \lambda_2 \nabla^2 b^{**} = \left[\frac{1}{r} - \frac{v_2}{2} (b^{**} - b + 1) \right] (b + b^{**} - 1) + 2b^{**}, \end{cases} \quad (16)$$

where the expressions in square brackets represent the nondimensional Ca^{2+} concentration. This system poses a challenge since it represents a non-linear and singular problem on an infinite domain. Further, most stationary approximations developed for the case of a simple 1:1 Ca^{2+} buffer cannot be extended to complex 2:1 Ca^{2+} buffers, with the exception of lowest-order RBA, which assumes that the reaction is at equilibrium in the entire domain (49). In Supporting Material 1 we derive RBA using the non-dimensionalization presented above, generalizing the expressions in (49). As is the case for a simple 1:1 Ca^{2+} buffer, RBA approximates the true solution very well within the parameter regime $\lambda_{1,2} \ll 1$ (26). However, this fast buffering condition has a complex interplay with the cooperativity condition $\varepsilon \ll 1$. In fact, the accuracy in buffer concentration estimation is significantly reduced with increasing Ca^{2+} binding cooperativity, corresponding to decreasing ε . Reducing the unbinding rate ratio γ along with ε partially rescues RBA accuracy (49). This very high sensitivity of RBA accuracy to buffering parameters calls for the development of new approximants. Below we present such new approximations, comparing and contrasting their accuracy to that of the RBA.

Note that the stoichiometric factors of 2 appearing in Eqs. 12-14, 16 could in principle be absorbed into the definitions of reaction rate parameters (45). However, we retain them, since this improves the consistency with the non-dimensionalization for the simple 1:1 buffer case adopted in (32, 38, 39), allowing to recover the latter simpler model as $\varepsilon \rightarrow 1$ and $\gamma \rightarrow 1$ (49).

In all results shown below, closed-form approximations to solutions of Eq. 16 are compared to the numerical solutions computed using the relaxation method and cross-validated using the shooting method; for the relaxation method we used CalC (Calcium Calculator) software, version 7.9.6 (<http://www.calciumcalculator.org>) (53).

RESULTS

Equilibrium Ca^{2+} nanodomain: power series interpolation method

We begin by presenting the power series interpolation method developed recently for the case of simple buffers with 1:1 Ca^{2+} binding stoichiometry (38, 39), which we will now generalize to the case of 2:1 Ca^{2+} buffers. This method involves finding simple *ansätze* that interpolate between the solution's Taylor series in powers of distance from the channel location, r , and the asymptotic power series expansion of the solution

in terms of the reciprocal distance from the channel location, $x=1/r$. We will refer to these two series as the short-range (low- r) and long-range (high- r) series.

We start with the non-dimensionalized form of the system for complex buffer, Eq. 16. This system has only a regular singularity at $r=0$ and does have a solution analytic at $r=0$, representing the physical nanodomain solution that we are seeking. Using the Frobenius-like approach we find the following Taylor series expansions in r for both b and b^{**} :

$$\begin{cases} b = b_0 + \varepsilon b_0 \lambda_1^{-1} r + O(r^2), \\ b^{**} = b_0^{**} + \frac{b_0^{**} + b_0 - 1}{2\lambda_2} r + b_2^{**} r^2 + O(r^3), \end{cases} \quad (17)$$

where the 2nd order coefficient in the expansion of b^{**} is given by

$$b_2^{**} = \frac{4b_0^{**} + v_2 \left[(1-b_0)^2 - (b_0^{**})^2 \right]}{12\lambda_2} + \frac{b_0^{**} + b_0 - 1}{12\lambda_2^2}. \quad (18)$$

In Eqs. 17,18, parameters b_0 and b_0^{**} represent concentrations of the free and the fully bound buffer at the channel location, $r=0$. These two values are finite and non-zero, but are *a priori* unknown characteristics of the underlying true solution, to be estimated by our approximation procedure. Because b_0 and b_0^{**} are unknown, Eq. 17 only provides the relationships between the coefficients of these Taylor expansions, rather than coefficients themselves. For example, denoting the 1st-order Taylor coefficients in Eq. 17 as b_1 and b_1^{**} , we obtain the constraints $b_1 = \varepsilon b_0 / \lambda_1$, and $b_1^{**} = (b_0^{**} + b_0 - 1) / (2\lambda_2)$, which we will use to determine some of the free parameters of each approximant considered below.

In order to obtain the long-range asymptotic series expansion of the solution, we make a coordinate mapping $x \equiv 1/r$, transforming Eq. 16 to the form

$$\begin{cases} \lambda_1 x^4 b_{xx} = 2\varepsilon b \left[x - \frac{v_2}{2} (b^{**} - b + 1) \right] + b + b^{**} - 1, \\ \lambda_2 x^4 b_{xx}^{**} = \left[x - \frac{v_2}{2} (b^{**} - b + 1) \right] (b + b^{**} - 1) + 2b^{**}. \end{cases} \quad (19)$$

This system has a unique asymptotic power series expansion near $x=0$ satisfying boundary conditions at $x \rightarrow 0^+$ (i.e. $r \rightarrow +\infty$), namely $b(x=0^+) = 1$, $b^{**}(x=0^+) = 0$. Up to terms of order x^3 , this asymptotic series expansion can be obtained by simply equating the right-hand sides of Eq. 19 to zero, which yields

$$\begin{cases} b = 1 - 2\varepsilon q x + \varepsilon q^2 \left[2q(1-2\varepsilon) - 1 \right] x^2 + O(x^3), \\ b^{**} = \varepsilon q^2 x^2 + 2\varepsilon q^3 \left[q(1-2\varepsilon) - 1 + \varepsilon \right] x^3 + O(x^4), \end{cases} \quad (20)$$

where we introduced the parameter $q = 1/(1 + \nu_1)$ for the sake of simplicity. It is important to note that the leading term in the $b^{**}(x)$ long-range expansion is of order $O(x^2)$, in contrast to b . This is intuitive, since the double-bound buffer state decays faster than $[\text{Ca}^{2+}]$ or $[\text{B}^*]$ as $[\text{Ca}^{2+}] \rightarrow 0$ with $x \rightarrow 0^+$ (i.e. as $r \rightarrow +\infty$). Note however that this is not the case when background $[\text{Ca}^{2+}]$ is not zero; this more general case is considered in Supporting Material 1. Parenthetically, we also note that the right-hand sides of Eq. 19 contain all reaction term, which RBA assumes to equal zero. Therefore, given that the left-hand side of Eq. 19 is of asymptotic order $O(x^4)$, Eq. 20 must agree up to the given order with RBA (38).

We will now consider simple *ansätze* whose series expansions simultaneously match leading terms of the low- r (short-range) series and the low- x (long-range, high- r) series given by Eqs. 17, 20. Inspired by the simple buffer case (39), we seek *ansätze* for b and b^{**} that combine Padé approximants (rational functions) and exponential functions, since they represent the simplest interpolants between the short-range and long-range power series expansions of the true solution described by Eqs. 17, 20. Below we list these *ansätze* for b and b^{**} , along with the corresponding short-range and long-range series representations. Our approximations are based on combinations of these *ansätze*, as summarized in Table 1. With a slight abuse of notation, we use the same function name (b or b^{**}) whether it is expressed as a function of distance r , or its reciprocal x .

First, we introduce an exponential *ansatz* for the free buffer concentration b , which depends on one free parameter A :

$$b(r) = 1 - 2\varepsilon q \frac{1 - e^{-r/A}}{r} = 1 - \frac{2\varepsilon q}{A} \left[1 - \frac{r}{2A} + O(r^2) \right], \quad (21)$$

$$b(x) \sim 1 - 2\varepsilon qx.$$

This *ansatz* automatically satisfies the term of order $O(x)$ in Eq. 20, $b \sim 1 - 2\varepsilon qx$. Matching the expansions of order $O(r)$ in Eq. 17, $b \sim b_0 + \varepsilon b_0 \lambda_1^{-1} r$, with the corresponding expansion in Eq. 21 leads to a quadratic equation for the spatial decay constant A , with the following positive root:

$$A = q\varepsilon + \sqrt{q^2 \varepsilon^2 + q\lambda_1} \quad (22)$$

We note that Eq. 21 captures the rigorous asymptotic behavior of the true solution in the simple 1:1 Ca^{2+} buffer case, which explains the good performance of this simple *ansatz* (39).

Next, we use one of the following two *ansätze* for the double-bound buffer concentration b^{**} :

1. Padé *ansatz* with two free parameters, β_1 and β_2 :

$$\begin{aligned}
b^{**}(r) &= \frac{\varepsilon q^2}{r^2 + \beta_1 r + \beta_2} \\
&= \varepsilon q^2 \left[\frac{1}{\beta_2} - \frac{\beta_1}{\beta_2^2} r + \frac{\beta_1^2 - \beta_2}{\beta_2^3} r^2 \right] + O(r^3), \\
b^{**}(x) &= \frac{\varepsilon q^2 x^2}{1 + \beta_1 x + \beta_2 x^2} = \varepsilon q^2 [x^2 - \beta_1 x^3] + O(x^4).
\end{aligned} \tag{23}$$

2. Exponential *ansatz* with one free parameter, s :

$$\begin{aligned}
b^{**}(r) &= \varepsilon q^2 \frac{1 - \exp(-sr)(1 + sr)}{r^2} \\
&= \varepsilon q^2 s^2 \left(\frac{1}{2} - \frac{s}{3} r + O(r^2) \right), \\
b^{**}(x) &\sim \varepsilon q^2 x^2.
\end{aligned} \tag{24}$$

We term the corresponding approximants as ExpPadé or ExpExp, with the former coming in two versions depending on how its parameters are constrained, ExpPadéA or ExpPadéB, as explained below (see Table 1). For each of the above *ansätze*, the non-dimensional Ca^{2+} concentration is determined using the conservation law in Eq. 12 (recall that we focus on the case $c_\infty=0$):

$$\begin{aligned}
c(r) &= \frac{1}{r} - \frac{v_2}{2} [1 - b(r) + b^{**}(r)], \\
c(x) &= x - \frac{v_2}{2} [1 - b(x) + b^{**}(x)].
\end{aligned} \tag{25}$$

Name	<i>Ansatz for b</i>	<i>Ansatz for b^{**}</i>	Parameters	<i>b^{**} accuracy</i>
ExpPadéA		$b^{**} = \frac{\varepsilon q^2}{r^2 + \beta_1 r + \beta_2}$	$\{A, \beta_1, \beta_2\}$	$O(r), O(x^3)$
ExpPadéB	$b = 1 - 2\varepsilon q \frac{1 - e^{-r/A}}{r}$			$O(r^2), O(x^2)$
ExpExp		$b^{**} = \varepsilon q^2 \frac{1 - e^{-sr}(1 + sr)}{r^2}$	$\{A, s\}$	$O(r), O(x^2)$

Table 1. List of the new approximants interpolating between the short-range and long-range series expansions in Eqs. 17, 20. All *ansätze* automatically match the term of order $O(x)$ in $b \sim 1 - 2\varepsilon q x$ and the term of order $O(x^2)$ in $b^{**} \sim \varepsilon q^2 x^2$. The corresponding Ca^{2+} concentration is given by Eq. 25. Parameter A in the b *ansatz* is found by matching terms of order $O(r)$ in Eq. 17, while the free parameters in the b^{**} *ansatz* ($\beta_{1,2}$ or s) are found by matching Eqs. 17, 20 up to orders indicated in the last column, which results in expressions shown in Table 2.

<i>Ansatz</i> name	Equations for <i>ansätze</i> parameters
All approximants	$A = q\varepsilon + \sqrt{q^2\varepsilon^2 + q\lambda_1}$
ExpPadéA	$\beta_1 = 2q[1 - q + \varepsilon(2q - 1)], \quad \beta_2 = \frac{1}{4}\left(Aq + \sqrt{A^2q^2 + 16A\beta_1q\lambda_2}\right)$
ExpPadéB	$\beta_1 = \frac{\beta_2}{2\lambda_2}\left(\frac{2\beta_2}{Aq} - 1\right), \quad 3\lambda_2\left(\frac{\beta_1^2}{\beta_2} - 1\right) + \beta_2^2\frac{2q-3}{2qA^2} + \frac{\beta_1}{2} - \beta_2 = \frac{q(q-1)}{4}$
ExpExp	$4\lambda_2s^3 + 3s^2 - 12/(qA) = 0$

Table 2. *Ansätze* parameters for the approximants shown in Table 1, as functions of model parameters $q, \varepsilon, \lambda_{1,2}$. For ExpPadéB and ExpExp, the value of β_2 or s is given by the real positive root of the given cubic equation, whose closed-form solutions are given in Appendix A.

Note that all of the *ansätze* for b and b^{**} are analytic at $r=0$, and that in the limit $r \rightarrow +\infty$ ($x=1/r \rightarrow 0^+$), they automatically match the leading non-zero term in the asymptotic series expansion of the solution given by Eq. 20: $b(x) \sim 1 - 2\varepsilon qx + O(x^2)$, $b^{**} \sim \varepsilon q^2 x^2 + O(x^3)$. Additionally, all *ansätze* satisfy appropriate physical constraints. Namely, imposing the condition $A > 0$ guarantees that the free buffer concentration b is positive and monotonically increasing to its maximal total value of 1 as $r \rightarrow +\infty$ for each *ansatz*. Further, b^{**} is also always positive given positive parameters β_1, β_2 , and s , and is monotonically decreasing to $b^{**}=0$ as $r \rightarrow +\infty$. This agrees with the fact that the fully bound buffer concentration is bounded and equals to zero infinitely far from the Ca^{2+} channel, where $[\text{Ca}^{2+}]=0$.

We match the free parameters in the above approximants following the same interpolation method as in the case of a simple 1:1 Ca^{2+} buffer (38, 39). Namely, the unknowns are b_0 and b_0^{**} in Eq. 17, plus either 2 or 3 parameters characterizing a particular approximant, as listed in Table 1. Therefore, 4 or 5 constraints are needed to find these unknowns. The first 4 constraints are obtained by matching the first two terms (of order $O(1)$ and $O(r)$) in the short-range series for both b and b^{**} , given by Eq. 17. For the 3-parameter ExpPadéA and ExpPadéB approximants, the final 5th constraint is needed, which comes from matching one additional term in the short- or the long-range series of b^{**} , as specified in the last column of Table 1. One obtains an algebraic system of 4 or 5 equations for the *ansatz* parameters, which are readily solvable in closed form.

Table 2 shows the exact expressions we obtain using this method for the free *ansatz* parameters in terms of the model parameters $\{\lambda_1, \lambda_2, q, \varepsilon\}$, except for β_2 in ExpPadéB and s in ExpExp, which are defined by solutions of cubic equations shown in this Table. The roots of these cubic equations are given in closed form in Appendix A. Once b and b^{**} are determined using these approximants, the partially bound buffer concentration b^* and Ca^{2+} concentration c can then be determined from b and b^{**} through conservation laws in Eqs. 12, 25.

We will now illustrate this series interpolation method more concretely using the ExpPadéA approximant as an example. This *ansatz* is formed by combining Eq. 21 for b and Eq. 23 for b^{**} . Then, as indicated in Table 1, we constrain the values of *ansatz* parameters using terms of orders $O(1)$ and $O(r)$ in Eq. 17 for both b and b^{**} , and the term of order $O(x^3)$ in Eq. 20 for b^{**} (recall that all *ansätze* automatically match the term of order $O(x)$ in b and the term of order $O(x^2)$ in b^{**}). Therefore, we obtain 5 constraints for 5 unknowns (three parameters in ExpPadéA *ansatz*, plus b_0 and b_0^{**}):

$$\begin{cases} b_0 = 1 - 2\varepsilon q / A, & b_0^{**} = \varepsilon q^2 / \beta_2, \\ \varepsilon b_0 / \lambda_1 = \varepsilon q / A^2, \\ (b_0^{**} + b_0 - 1) / (2\lambda_2) = -\varepsilon q^2 \beta_1 / \beta_2^2, \\ \varepsilon q^2 \beta_1 = 2\varepsilon q^3 [1 - q + \varepsilon(2q - 1)]. \end{cases} \quad (26)$$

The 2nd and 3rd equations in this system lead to quadratic equations for A and β_2 , whose solutions are given in Table 2. Derivation of ExpPadéB approximant is similar, except that the term of order $O(r^2)$ in Eq. 17 is used instead of the term of order $O(x^3)$ in Eq. 20, resulting in a cubic equation for parameter β_2 shown in Table 2.

Accuracy in approximating buffer and Ca^{2+} concentrations

As a crude demonstration of the performance of our new *ansätze*, Figure 1 shows our approximants for 4 select combinations of model parameters, with each column presenting the results for all concentration variables (b, b^*, b^{**} , and c), for a particular set of values of λ_2, ν_2, γ , and ε , as labeled in the panel titles. The accurate numerical results are shown as thick grey curves. Since the expressions for the free buffer b are identical for ExpPadéA, ExpPadéB and ExpExp approximants, they are shown as a single *dashed magenta curves* in the top panels. RBA is only shown for the parameter combination corresponding to the last two columns of Fig. 1, since it is too inaccurate for the other two parameter sets.

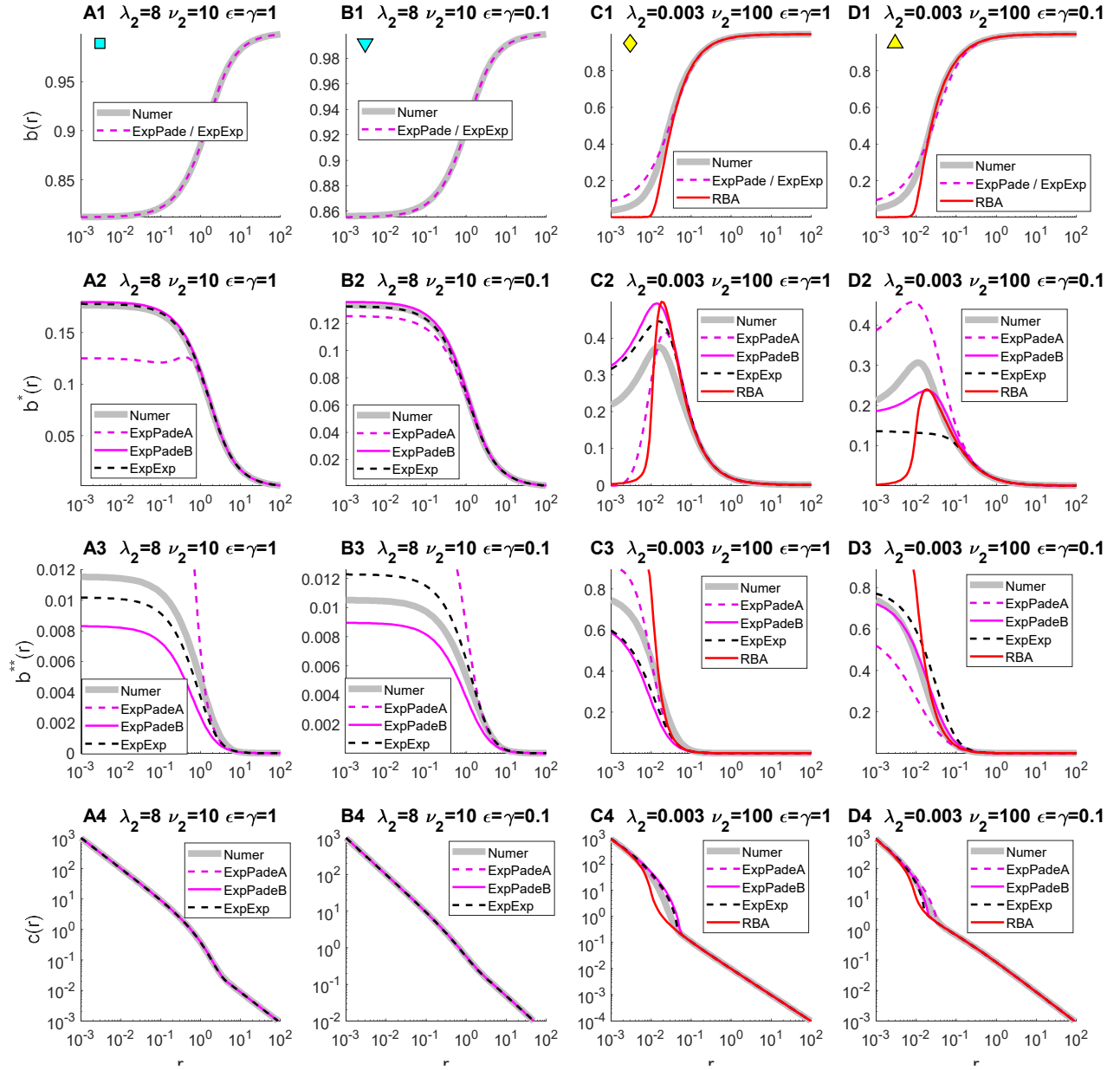


FIGURE 1. Approximations of equilibrium free buffer (top row), partially bound buffer (2nd row), fully bound buffer (3rd row) and Ca^{2+} concentrations (bottom row), as functions of distance from the Ca^{2+} channel, for 4 distinct choices of model parameters λ_2 , ν_2 , γ , and ϵ indicated in the panel titles. The distinct curves mark the series interpolants shown in Table 1: ExpPadéA (*magenta*), ExpPadéB (*dashed magenta*), ExpExp (*dashed black*), and RBA (*red*). RBA is not shown for the first two parameter combinations (A1-B4) due to poor performance. *Grey curves* show the accurate numerical simulations. The accuracy of some approximants is sufficiently high for the curves to completely overlap with the numerical solution on the given scale, and hence the difference between the curves is hard to resolve by eye.

As will be elucidated further below (see Figs. 3-6), the parameter regimes we selected in Fig. 1 are not optimal for the *ansätze* we introduce. Nevertheless, even for the chosen sub-optimal parameter combinations, a decent qualitative agreement with the accurate numerical solution is achieved by at least one of the *ansätze*, with higher accuracy achieved for the first two parameter combinations in Fig. 1A1-4, B1-4. We observe that RBA can compete with the newly presented approximants only when diffusivity λ_2 is very small (Fig. 1C1-C4); therefore, RBA is not shown for the other three parameter choices. Note the difference in scales in the different panels of Fig. 1: some of the apparent large discrepancies for b^* and b^{**} involve relatively small absolute differences. The accuracy of several of the newly presented approximants is sufficiently high for the curves to completely overlap with the numerical simulations. Therefore, the series interpolation method achieves significant improvement of approximation accuracy for a wide range of model parameters, as compared to RBA.

It is interesting to note that the partially-bound buffer concentration b^* is not necessarily monotonic with respect to distance from the channel location, unlike the free and fully-bound concentration variables. Despite the simple functional forms of our *ansätze*, they do in fact reproduce this non-monotonic behavior: see for instance the ExpPadéB approximant in Fig. 1C2,D2.

Figure 1 shows that the new approximants give consistently accurate results, at least for the examined parameter sets. As in the simple buffer case, buffer approximations have the lowest accuracy near the channel, and the greatest accuracy far from the channel, since buffer concentrations at the channel location are unknown, whereas the long-range asymptotic behavior of the true solution is known, and given by Eq. 20. In contrast, the differences between distinct Ca^{2+} approximations and the numerical solution are shown on a logarithmic scale, and are more pronounced at intermediate distances from the channel, due to the dominance of the free source term $1/r$ near the channel (Eq. 25). Since the $[\text{Ca}^{2+}]$ traces shown in the last row of panels in Fig. 1 are obtained from the Ca^{2+} conservation law in Eq. 25 using inexact approximations for b and b^{**} , no direct physical constraints on Ca^{2+} were imposed. For specific parameters regimes, this may result in negative values of $[\text{Ca}^{2+}]$ sufficiently far from the channel, where the corresponding true concentration values are small. This indeed happens for very large values of buffering strength, $\nu_{1,2} \geq 100$. When this occurs, we use the RBA approximation derived in (49) and generalized in Supporting Material 1 as a lower bound on Ca^{2+} , since RBA is very accurate sufficiently far from the channel for any model parameter values, as we noted above. Moreover, our extensive numerical investigation leads us to conjecture that RBA in fact represents a sub-solution (a pointwise lower bound) for the true $[\text{Ca}^{2+}]$. This imposed truncation of $[\text{Ca}^{2+}]$ from below using RBA helps us correct the errors in estimating Ca^{2+} at larger

distances when buffering is very strong (see for instance Fig. 1C4). Even in such cases where negative $[\text{Ca}^{2+}]$ values are replaced with the corresponding RBA values at large distances, the accuracy of the new approximants at closer distances are significantly better than RBA accuracy, as is the case for instance for the parameters in Fig. 1C4.

Examining approximation behavior for several example parameters combinations is insufficient to unveil the complicated parameter-dependent accuracy of these approximations. Therefore, following prior work (32, 38, 39, 49), we will now systematically explore the parameter-dependence of the absolute deviation between the given approximation and the accurate numerical solution, using the following norm, similar but slightly different from the norm used in the case of simple buffer (38, 39):

$$\begin{aligned} \|b_{appr} - b_{num}\| &= \frac{2}{N p} \sum_{n=1}^N |b_{appr}(r_n) - b_{num}(r_n)|, \\ p &= \max_{n=1..N} |b_{appr}(r_n)| + \max_{n=1..N} |b_{num}(r_n)|, \\ r_n &= 10^{-3+5n/N}, \quad n = 1, 2, \dots, N. \end{aligned} \quad (27)$$

The deviations are computed on a set of $N=100$ points spanning 5 orders of magnitude of distance r , from 10^{-3} to 10^2 , on a logarithmic scale. Therefore, apart from the normalization factor p in the denominator (explained below), these are effectively L^1 norms weighted by $1/r$, which requires a lower distance cut-off, set to $r_{\min}=10^{-3}$. The heavier weighting of short distances is justified by two reasons: (1) as we mentioned, our method has the greatest error at the channel location, and (2) the accuracy close to the channel is more important for actual biophysical modeling applications. We use the same error measure for approximating bound buffer state b^{**} as for b . Given the difference in absolute magnitude of b^{**} and b , we normalize by the maximal concentration p in the denominator of Eq. 27 to make it an even more stringent accuracy measure: as Fig. 1 illustrates, b^{**} can be quite small in certain parameter regimes, as compared to the free buffer b , which always approaches 1 as $r \rightarrow +\infty$.

Since b^* and c are uniquely determined by b and b^{**} through the two conservation laws in Eqs. 12, 25, in all figures below we will examine the sum of errors for b and b^{**} , instead of analyzing the accuracy of these two concentration fields individually. In Figure 2 we show a systematic comparison of the accuracy of the new approximants by plotting such sum of errors in b and b^{**} for each approximant as a function of the buffering strength parameter ν_2 varying from 10^{-3} to 10^3 , for three different fixed values of the buffer diffusivity parameter λ_2 ($\lambda_2=0.1$, $\lambda_2=1$, or $\lambda_2=10$) and two combinations of cooperativity parameters (ε, γ) . To reveal the impact of Ca^{2+} -binding cooperativity on approximant performance, one choice of (ε, γ) values corresponds to a non-cooperative buffer ($\varepsilon=\gamma=1$, Fig. 2A2,B2,C2), while the other choice corresponds to a

very cooperative buffer ($\varepsilon=\gamma=0.1$, Fig. 2A1,B1,C1). Combining the error measures of b and b^{**} allows us to choose a single best approximation for each given parameter combination. The error of RBA (red curves) is also included for the sake of comparison.

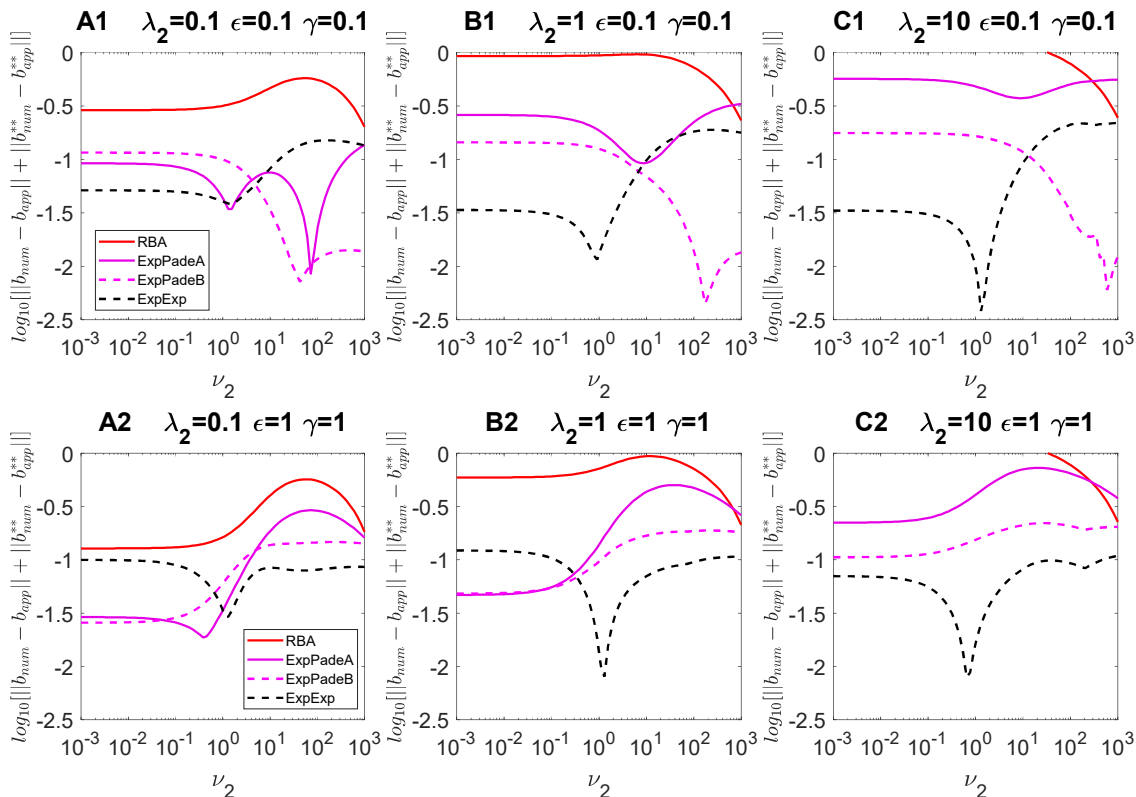


FIGURE 2. Accuracy comparison of the series interpolant approximations for the equilibrium free and fully bound buffer concentrations: ExpPadéA (magenta), ExpPadéB (dashed magenta), and ExpExp (dashed black). RBA error is also plotted for comparison (red curves). All panels show the \log_{10} of the sum of average errors of approximating concentrations of free buffer (b) and fully bound buffer (b^{**}) computed using Eq. 27, as a function of buffering strength ν_2 ranging from 10^{-3} to 10^3 , for 3 distinct choices of parameters λ_2 , ε and γ .

For most combinations of parameters examined in Fig. 2, the new approximants outperform RBA quite significantly, confirming the results shown in Fig. 1. In the non-cooperative buffer case $\varepsilon=\gamma=1$ (bottom row of panels in Fig. 2), for sufficiently large values of ν_2 and λ_2 the best approximating method is always ExpExp, and its average relative error is always below 10%. This level of accuracy is very good given such a simple approximation and such a stringent error measure. In the cooperative buffer case, $\varepsilon=\gamma=0.1$ (top row of panels in Fig. 2), the individual error curves are more tangled, and the choice of best method is somewhat more complicated. However, in general ExpExp achieves superior accuracy at smaller values of buffering strength ν_2 , whereas ExpPadéB becomes superior for larger values of ν_2 . Although RBA performs

poorly relative to other approximants for parameter conditions examined in Figure 2, the advantage of RBA for smaller values of $\lambda_{1,2}$ will be revealed in the results presented next.

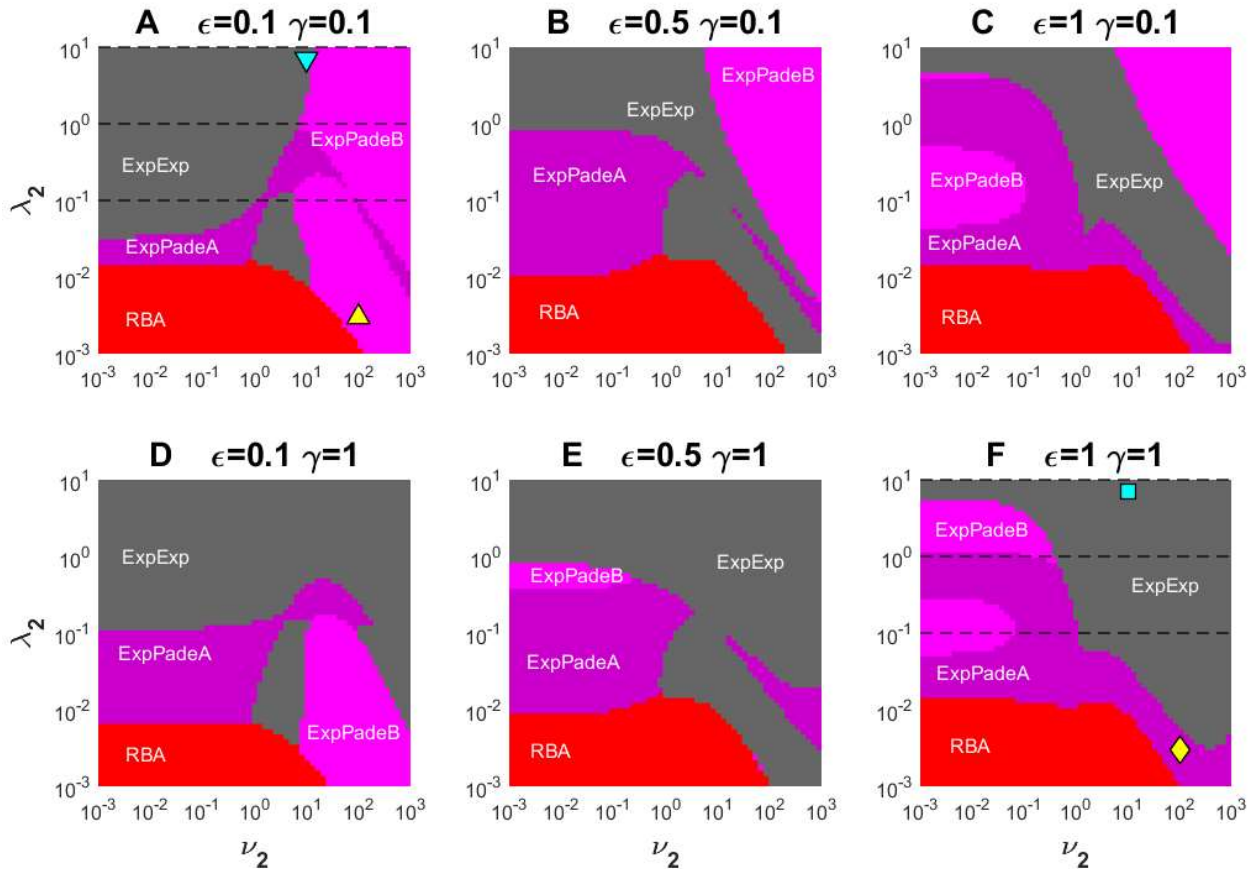


FIGURE 3. Comparison of parameter regions where a given approximant outperforms the rest in estimating the combined errors of free and fully bound buffer concentration approximations in the (ν_2, λ_2) parameter plane, according to the error measure given by Eq. 27, with 6 different choices of cooperativity parameters ε and γ : (A) $\varepsilon=\gamma=0.1$; (B) $\varepsilon=0.5, \gamma=0.1$; (C) $\varepsilon=1, \gamma=0.1$; (D) $\varepsilon=0.1, \gamma=1$; (E) $\varepsilon=0.5, \gamma=1$; (F) $\varepsilon=\gamma=1$. Each color in A through F marks the parameter region of best performance for the following approximants: RBA (red), ExpPadeA (dark magenta), ExpPadeB (light magenta), and ExpExp (gray). Yellow and cyan symbols mark parameter point corresponding to simulations in Figure 1. Dashed lines mark the locations of parameter scans in Figure 2.

Figure 3 summarizes and extends the results presented in Fig. 2, labeling the best approximants for a wide range of buffer mobility λ_2 varying over 4 orders of magnitude, and buffering strength ν_2 varying over 6 orders of magnitude, for 6 fixed sets of cooperativity parameters ε and γ corresponding to each of the 6 panels. The selection of best approximant in Fig. 3 is based on the minimal sum of errors of b and b^{**} approximations; the corresponding smallest error value is shown in Fig. 4. As noted above, using this combined error measure helps in determining the single best approximation method for a given set of model

parameters, recalling that b^* and c are uniquely determined by b and b^{**} (Eqs. 12, 25). Figure 3 shows that there is still a significant portion of parameter space where RBA outperforms our newly developed methods, but as expected, this only happens for sufficiently small values of λ_2 . As Fig. 4 illustrates, a qualitative accuracy within 10% is always guaranteed for all examined parameter combinations, and for some narrow parameter regimes the accuracy can be extremely high, with the average combined error measure reaching 0.025%.

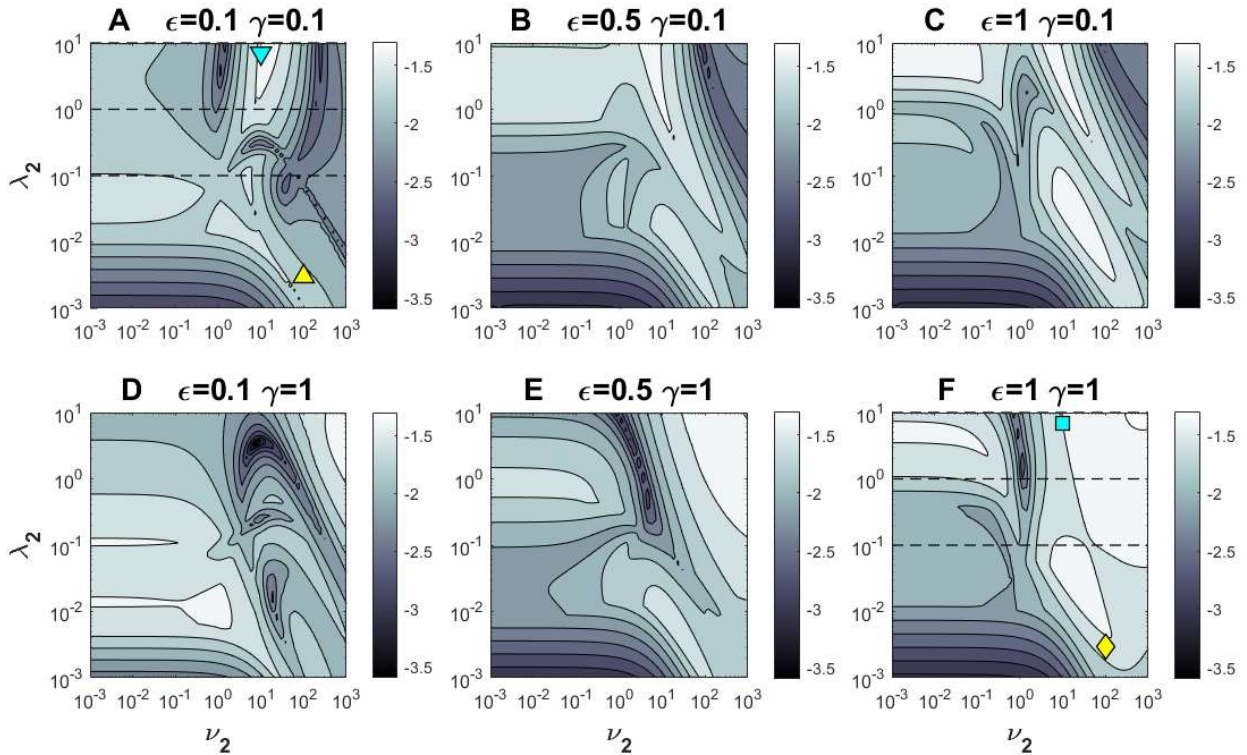


FIGURE 4. The smallest error in estimating the free and fully bound buffer concentrations in the (ν_2, λ_2) parameter plane, according to the error measures given by Eq. 27, with ε and γ fixed to 6 different choices, as in Figure 3. The gray-scales in A through F indicate the \log_{10} of the sum of average errors of the free and the fully bound buffer approximations (Eq. 27). Darker shades represent better accuracy, according to the error bars to the right of each panel.

Even though Ca^{2+} is uniquely determined from the buffer concentrations by the Ca^{2+} conservation law, it is still useful to look at the performance of different approximants in estimating $[\text{Ca}^{2+}]$ separately, since the latter is of obvious physical importance and has a different behavior as a function of distance from the channel. As noted above, close to the channel location $[\text{Ca}^{2+}]$ is dominated by the source term, $1/r$, therefore we will modify the buffer error norm, Eq. 27, by taking the logarithm of $[\text{Ca}^{2+}]$ (38, 39, 49):

$$\|c_{appr} - c_{num}\| = \frac{1}{N} \sum_{n=1}^N \left| \ln c_{appr}(r_n) - \ln c_{num}(r_n) \right|, \quad (28)$$

$$r_n = 10^{-3+5n/N}, \quad n = 1, 2, \dots, N.$$

We note that qualitatively this norm has the same behavior as the relative norm used in (32). Figure 5 labels the approximants which minimize this error in estimating $[Ca^{2+}]$, with the corresponding error value shown in Fig. 6, using the same parameter combinations as in Figs. 3 and 4. Figure 5 shows that for any particular set of model parameters, the optimal approximants for $[Ca^{2+}]$ can be different from the optimal buffer approximant shown in Fig. 3, despite the fact that $[Ca^{2+}]$ is directly calculated from buffer concentrations. As discussed above, $[Ca^{2+}]$ approximant performance is more sensitive to its accuracy at intermediate distances, in contrast to the buffer error measure, which is the greatest in the channel vicinity. Therefore, the error in Ca^{2+} estimation measures the accuracy of our approximants at intermediate distance from the channel, while the error in buffer estimation reveals the method accuracy proximal to the channel location. This fact can also be observed in Figure 1. Finally, we note that the uneven boundaries between accuracy levels in Fig. 6 are not numerical artifacts, but reflect the complicated shape of the boundaries of optimal performance regions shown in Fig. 5.

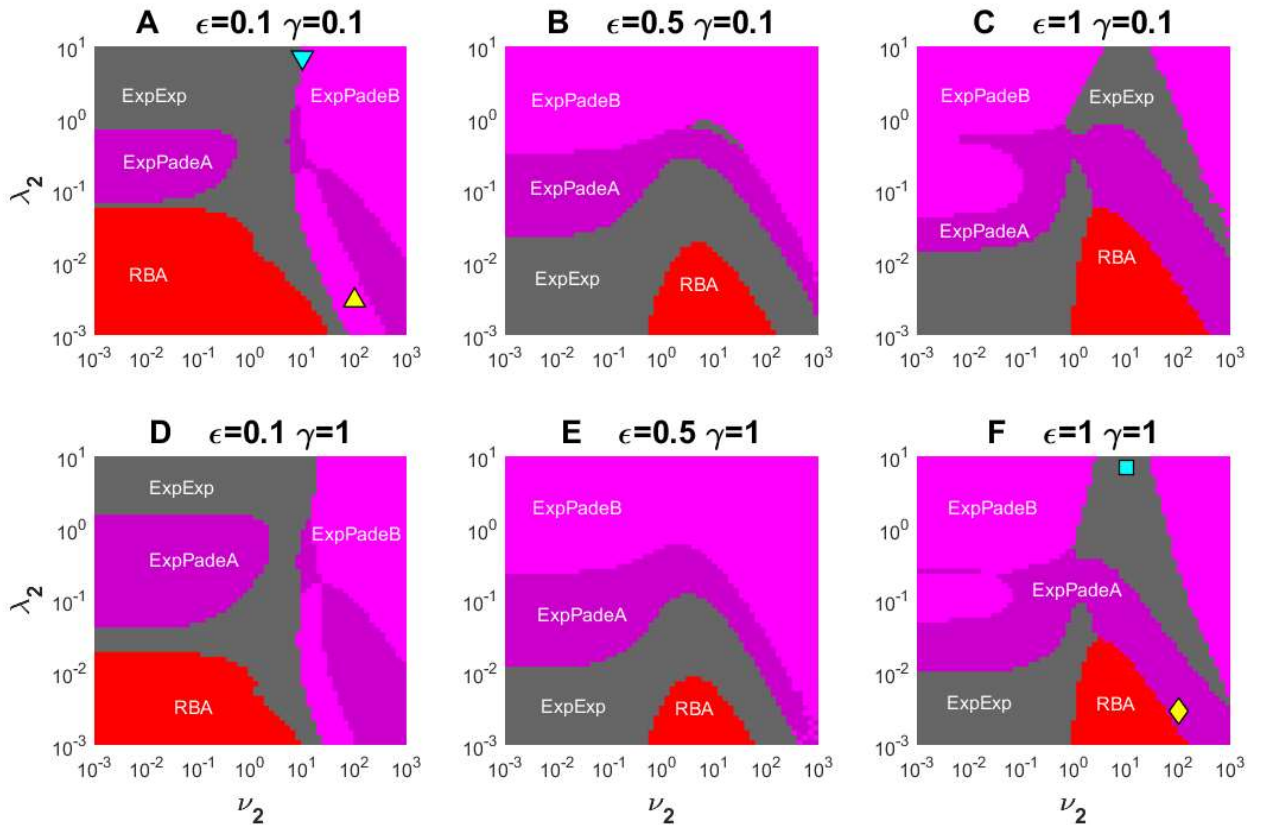


FIGURE 5. Comparison of parameter regions where a given approximant outperforms the rest in estimating $[Ca^{2+}]$ in the (ν_2, λ_2) parameter plane, according to the error measure given by Eq. 28, with ε and γ fixed to 6 different choices, as in Figure 3. Each color in A through F marks the parameter region of best performance for the following approximants: RBA (*red*), ExpPadéA (*dark magenta*), ExpPadéB (*light magenta*), and ExpExp (*gray*). Yellow and cyan symbols mark parameter points corresponding to simulations in Figure 1.

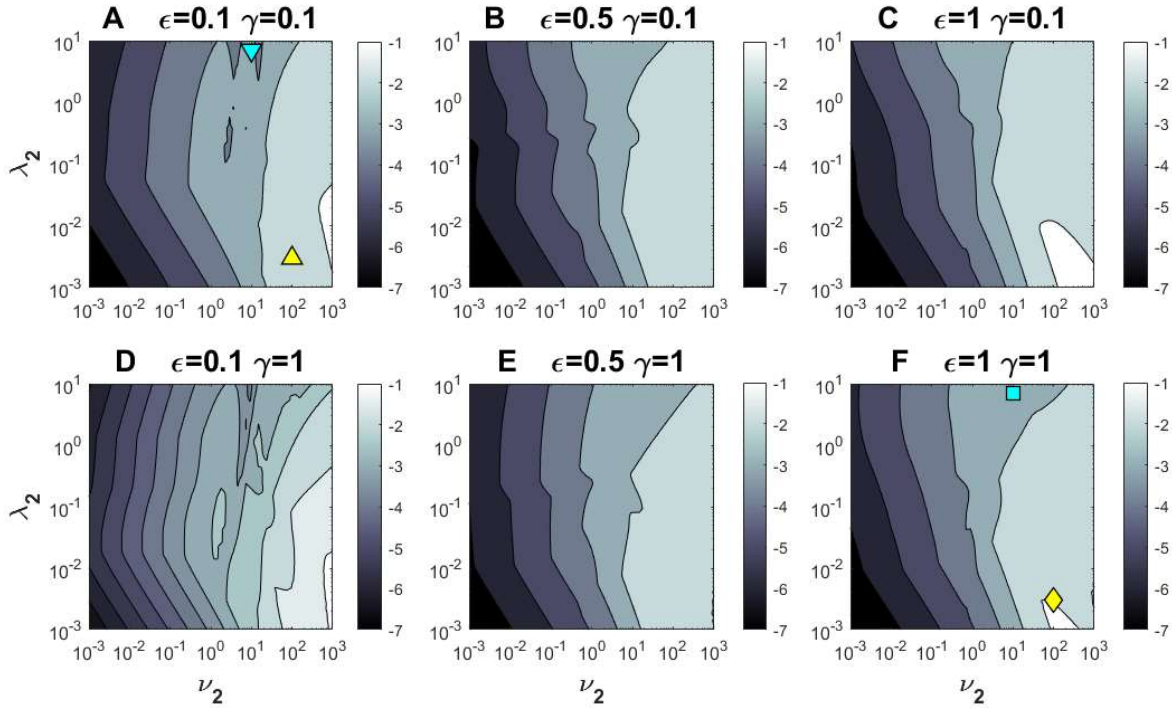


FIGURE 6. The error in estimating $[Ca^{2+}]$ in the (ν_2, λ_2) parameter plane, obtained using the best approximant shown in Figure 5 for each parameter point, with ε and γ fixed to 6 different choices, as in Figure 5. All parameter choices and panel layout are identical with Figures 3-5. The grayscale in all panels indicates the \log_{10} of error value given by Eq. 28, as indicated in scale bars to the right of each panel. Darker shade represents better accuracy.

Finally, in order to evaluate whether our newly developed approximants achieve sufficient accuracy for parameters corresponding to real biological buffers, in Figure 7 we simulate the Ca^{2+} nanodomains in the presence of $100\mu M$ of Ca^{2+} buffer with the properties of either calretinin or one of the two lobes of calmodulin, shown in Table 3. For calretinin, we use parameter values reported by Faas et al. (42), while for calmodulin, we use reaction parameters that were carefully compiled from multiple biochemical studies by Ordyan et al. (52). As Figure 7 reveals, our newly developed method, ExpPadéA and ExpPadéB, work remarkably well for N-lobe or C-lobe of calmodulin: the curves for b , b^{**} , and c corresponding to the approximations and the numerical simulations completely overlap at the chosen ordinate scale. For calretinin, ExpPadéB works the best, and demonstrates very reasonable accuracy. Although ExpPadéB fails

to accurately describe the behavior of the single-bound calretinin concentration, it does capture the order of magnitude of this concentration variable; note also that the latter is much smaller than b and b^{**} .

Although the approximants we present do not allow to model the simultaneous impact of both lobes of calmodulin, since this would require generalizing our approach to buffer with 4 binding sites, the results obtained for the N-lobe alone are of value, since the N-lobe has much faster kinetics, and would reach a quasi-equilibrium state on short time scales compared to the much slower C lobe.

Parameter	$k_1^+ (\mu M ms)^{-1}$	$k_2^+ (\mu M ms)^{-1}$	$K_1 (\mu M)$	$K_2 (\mu M)$	$\varepsilon = \frac{K_2}{K_1}$	$\gamma = \frac{k_2^-}{k_1^-}$	λ_2	ν_2
CaR coop. sites	0.0018	0.31	28	0.068	$2.4 \cdot 10^{-3}$	0.42	$1.6 \cdot 10^{-3}$	294
CaR non-coop.site	0.0073	--	36	--	--	--	--	--
CaM N-lobe	0.1	0.15	26.6	6.6	0.248	0.372	0.323	3.03
CaM C-lobe	0.004	0.01	10	0.93	$9.3 \cdot 10^{-2}$	0.23	0.68	21.5

Table 3. Ca^{2+} binding properties of strongly cooperative buffers calretinin (CR) and calmodulin (CaM), as reported in (42, 52). Each CR molecule contains 5 binding sites, consisting of two identical cooperative pairs of Ca^{2+} -binding sites and one independent non-cooperative site. CaM molecule consists of two independent domains (lobes), each binding two Ca^{2+} ions in a cooperative manner. Values of λ_2 and ν_2 are calculated for Ca^{2+} current strength of $I_{Ca}=0.4$ pA, total buffer concentrations of $B_T=100 \mu M$, buffer- Ca^{2+} mobility ratio of $D_B/D_{Ca}=0.1$, and $D_{Ca}=0.2 \mu m^2/ms$.

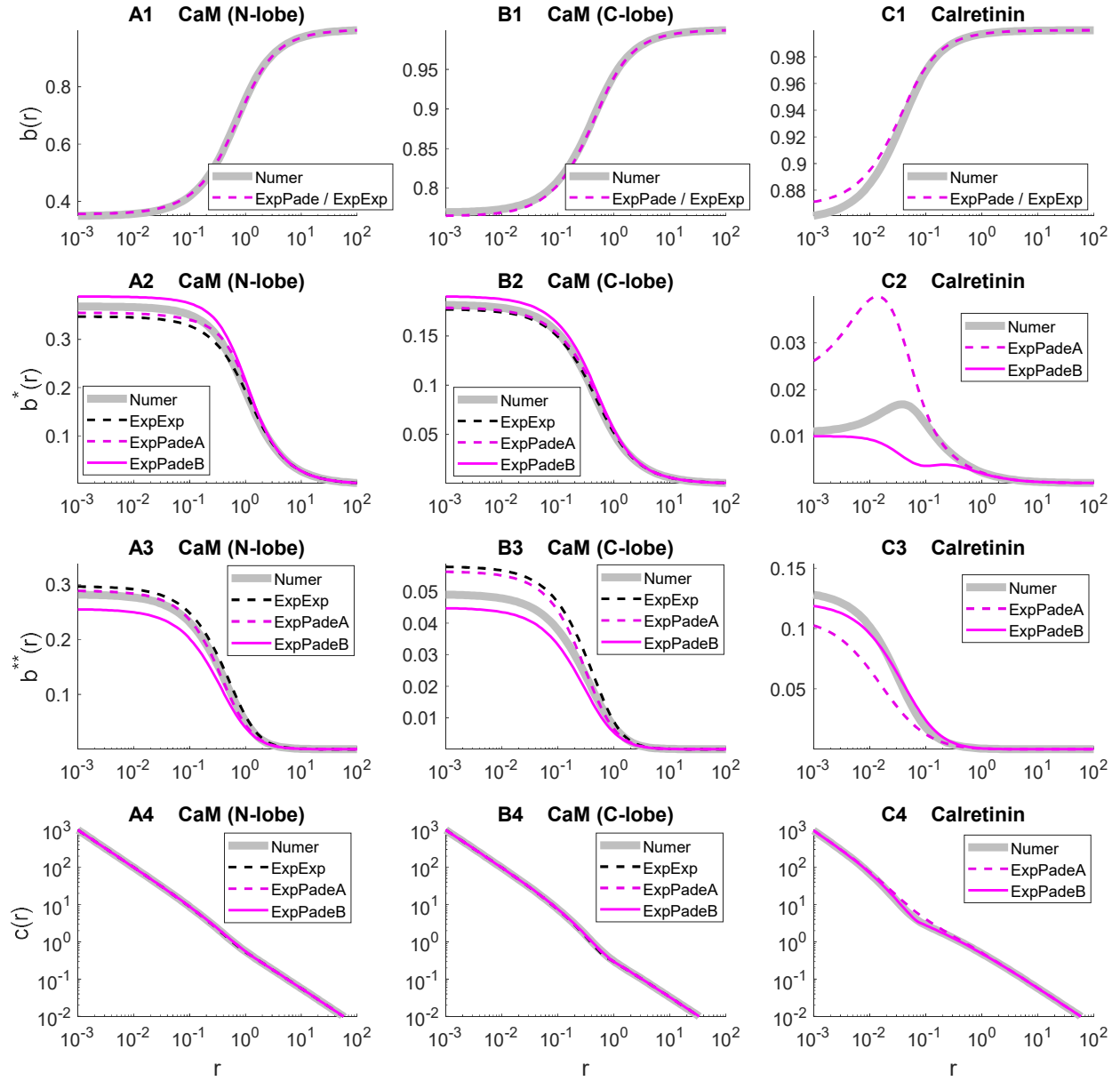


FIGURE 7. Approximation performance for biological buffers: calmodulin N-lobe (A1-A4), calmodulin C-lobe (B1-B4), and calretinin (C1-C4). Parameters values are in Table 3, corresponding to the current of $I_{Ca}=0.4$ pA, and total buffer concentration of $100 \mu\text{M}$. Only the best approximations are shown: ExpPadeA (solid magenta curve), ExpPadeB (dashed magenta), and ExpExp (dashed black). Accurate numerical results are shown as thick gray curves.

DISCUSSION

We demonstrated that the series interpolation approach introduced for the case of 1:1 Ca^{2+} buffers in (38,39) can be extended to buffers with 2:1 Ca^{2+} -binding stoichiometry, and we presented several simple but accurate interpolants that combine rational and exponential functions. As summarized in Figs. 3-6, and Fig. S1 of the Supporting Material 1, these new approximants achieve reasonable accuracy in estimating equilibrium buffer and Ca^{2+} concentrations near an open Ca^{2+} channel in a wide range of relevant model parameters. RBA, the only other previously developed method applicable to 2:1 buffers, is nevertheless still superior for very small values of non-dimensional mobility parameters $\lambda_{1,2}$. However, our new approximants have more uniform accuracy compared to RBA over a wide range of several orders of magnitude in the relevant dimensionless parameters λ_2 , ν_2 , γ , and ε . As Figure 4 shows, the average combined error for the free and fully bound buffer concentrations is within 10% for all examined parameter combinations for the new approximants. Fig. 6 demonstrates similar maximal error in estimating Ca^{2+} , albeit requiring truncation at large distances to ensure the physical constraints $[\text{Ca}^{2+}] > 0$ for large values of buffering strength. Further, Figure 7 shows that good qualitative agreement can be achieved even with more extreme model parameter values corresponding to calretinin or one of the two lobes of calmodulin, which correspond to parameter combinations shown in Table 3. Figures 2-6 demonstrate that the accuracy profile of the approximants we introduced is highly non-trivial, with the error measure exhibiting large dips for certain parameter combinations. This is of potential interest and may reveal interesting properties of the underlying true solutions, deserving a careful investigation in the future.

Several functional forms other than the ones shown in Table 1 were considered, but are not presented here due to either insufficient performance or lack of closed-form solutions for parameters. However, given the simplicity of the interpolating approximants we presented, improved *ansätze* could potentially still be found. This is particularly likely for the case of non-zero background Ca^{2+} concentration examined in Supporting Material 1: only the simplest lowest-order interpolating approximants were considered in the latter general case.

Of course, practical use of the proposed approximants requires an algorithm for the choice of a particular *ansatz*, given a particular set of model parameters, without knowing the exact solution. In Supporting Material 2, we provide simple and concise MATLAB code that selects the best approximants as a function of 4 model parameters, based on shallow neuronal networks with only 9 or 13 hidden nodes, pre-trained with data shown in Figs. 3,5. The resulting algorithms capture very well the nontrivial topology of parameter space segmentation shown in Figs. 3,5.

There are many directions for possible extensions and improvements of this work. For example, our approximants are only applicable to a single channel and a single 2:1 Ca^{2+} buffer, whereas RBA allows an extension to an arbitrary number of channels and buffers (although the latter requires considerable increase in complexity). We note however that the methods we presented could be extended to the case of two distinct 1:1 Ca^{2+} buffers. We should also mention that we did not consider any Ca^{2+} sinks and the effect of finite channel pore radius. Including a linear homogeneous Ca^{2+} uptake mechanisms, along the lines of (21), would greatly improve the utility of the developed approximations. Finally, we should note that the study of equilibrium nanodomains implicitly assumes that the steady-state is established very quickly and ignores transient dynamics before the equilibrium is reached. However, this is not always the case (19). We note that the quality of this equilibrium assumption is not determined by the parameters defined in Eq. 14-15, but strongly depends on one additional nondimensional parameter given by the product of the channel opening time and one of the buffers' two Ca^{2+} unbinding rates, $k_{1,2}^-$. It is guaranteed that for some combinations of these five parameters the equilibrium assumption will be a very accurate one, while for other combinations the equilibrium will not be achieved sufficiently fast on the time scale of the channel opening time. Therefore, the characteristic time needed to reach the steady state should be properly examined for a wide range of parameter values in future work. Some related work concerning transients dynamics in reaction-diffusion systems can be found in (54-58). More generally, the fundamental mathematical analysis for the complex buffer case, along the lines of analysis in (39), is yet to be performed. For instance, we did not give a rigorous proof that RBA provides a sub-solution for $[\text{Ca}^{2+}]$ in this problem. Finally, we only considered the series interpolation method, whereas the feasibility of extending the variational method introduced in (39) to the case of 2:1 Ca^{2+} buffers is still an open question, to be explored in future work. One could explore in particular the applicability of the multifunction variational method described in (59).

The newly developed approximants can be used to study in detail the parameter dependence of equilibrium concentrations of Ca^{2+} and distinct buffer states, which can be quite non-trivial for a buffer with two binding sites. For example, the results shown in Figure 1 already reveal an interesting non-monotonic dependence of single-bound buffer on the distance from the Ca^{2+} channel for some, but not all, model parameters. To our knowledge, this non-monotonic behavior has not been previously noted. Since most buffers have dual Ca^{2+} buffering and sensing roles, with partially and fully bound buffer having distinct affinities to downstream biochemical targets (40, 41, 48), this non-trivial property of the equilibrium solution may be of potential physiological significance, to be analyzed in detail. Non-trivial effects of cooperative Ca^{2+} binding by biological buffers with multiple Ca^{2+} binding sites have also been pointed out

by prior modeling studies. For example, it has been shown that cooperative Ca^{2+} buffers decrease the facilitation of Ca^{2+} transients associated with buffers saturation (40, 45), but may increase short-term synaptic facilitation through the mechanism of buffer dislocation (60). This is directly related to the interesting fact that the buffering capacity of a cooperative Ca^{2+} buffer increases with increasing background Ca^{2+} concentration, which may play an important homeostatic role (42, 45, 49). On longer time scales, Kubota and Waxham (47) showed the interesting “hand-off” of Ca^{2+} from the N-lobe to the C-lobe of calmodulin upon channel closing, and the intricate dependence of each lobe’s Ca^{2+} saturation on the Ca^{2+} influx amplitude and duration. More generally, cooperative Ca^{2+} binding by calmodulin and the resulting activation of downstream biochemical pathways plays important roles in the regulation of long-term synaptic plasticity and other fundamental cell processes (43-47, 52, 61-63). Deeper understanding of Ca^{2+} dynamics in the presence of cooperative buffers may also be important for an accurate interpretation of optogenetic measurements with genetically-encoded fluorescent Ca^{2+} dyes, which are formed by fusing a calmodulin molecule with a green fluorescent protein (64). All this underscores the importance of modeling and analysis of Ca^{2+} binding by buffers and sensors with multiple Ca^{2+} binding sites.

Author Contributions

V.M. conceived, designed, and supervised this research project; Y.C. and V.M. both performed model analysis, coding, numerical simulations and analysis of results, and both took part in the writing of the manuscript.

Acknowledgements

This work was supported in part by NSF grant DMS-1517085 to V.M. The authors acknowledge valuable discussions with Cyrill Muratov (NJIT) and Arthur Sherman (NIDDK, NIH).

APPENDIX A: Approximation Parameters, Zero Background Ca^{2+} Concentration

For the **ExpPadéB** approximation, matching the coefficients of the short- and long-range series expansions given by Eqs. 17, 20 leads to cubic systems for the *ansatz* parameter β_2 shown in Table 3, with the following explicit solution:

$$\beta_2 = q(Y + G + F/G). \quad (29)$$

The auxiliary quantities Y, G, F are determined by

$$\begin{aligned} G &= \left(\sqrt{E^2 - F^3} + E \right)^{1/3}, \\ E &= Y^3 - YW + \lambda_2 X / 24, \\ F &= Y^2 - 2W/3, \\ X &= A^2 (q - 1 + 12\lambda_2 q^{-1}), \\ Y &= [5A + \lambda_2 (3 - 2q)] / 18, \\ W &= A^2 (1 - 2\lambda_2) / 12. \end{aligned} \quad (30)$$

For the **ExpExp** approximation, the explicit solution of *ansatz* parameter s has the form

$$s = G - Y + Y^2/G, \quad (31)$$

where the auxiliary quantities G and Y are determined by

$$\begin{aligned} G &= \left(\sqrt{E^2 - Y^6} - E \right)^{1/3}, \\ E &= Y [Y^2 - 6/(Aq)], \\ Y &= 1/(4\lambda_2). \end{aligned} \quad (32)$$

In both of these approximants, the value of *ansatz* parameter A is given by Eq. 22. All fractional powers should be understood as principal roots, as implemented in MATLAB. Supporting Material 2 contains simple MATLAB code computing and plotting these expressions.

REFERENCES

1. Berridge, M.J., P. Lipp, and M.D. Bootman. 2000. The versatility and universality of calcium signalling. *Nat. Rev. Mol. Cell. Biol.* 1: 11–21.
2. Augustine, G.J., F. Santamaria, and K. Tanaka. 2003. Local calcium signaling in neurons. *Neuron.* 40: 331–346.
3. Oheim, M., F. Kirchhoff, and W. Stühmer. 2006. Calcium microdomains in regulated exocytosis. *Cell Calcium.* 40: 423–439.
4. Konieczny, V., M.V. Keebler, and C.W. Taylor. 2012. Spatial organization of intracellular Ca²⁺ signals. *Semin. Cell Dev. Biol.* 23: 172–180.
5. Stanley, E.F. 2016. The Nanophysiology of Fast Transmitter Release. *Trends Neurosci.* 39: 183–197.
6. Wang, L.-Y., and G.J. Augustine. 2015. Presynaptic nanodomains: a tale of two synapses. *Front. Cell. Neurosci.* 8: 1496.
7. Matveev, V., R. Bertram, and A. Sherman. 2011. Calcium cooperativity of exocytosis as a measure of Ca(2)⁺ channel domain overlap. *Brain Res.* 1398: 126–138.
8. Eggermann, E., I. Bucurenciu, S.P. Goswami, and P. Jonas. 2012. Nanodomain coupling between Ca(2)⁽⁺⁾ channels and sensors of exocytosis at fast mammalian synapses. *Nat. Rev. Neurosci.* 13: 7–21.
9. Kim, M.H., G.L. Li, and H. von Gersdorff. 2013. Single Ca²⁺ channels and exocytosis at sensory synapses. *J. Physiol.* 591: 3167–3178.
10. Bornschein, G., and H. Schmidt. 2019. Synaptotagmin Ca²⁺ Sensors and Their Spatial Coupling to Presynaptic Cav Channels in Central Cortical Synapses. *Front. Mol. Neurosci.* 11: 796.
11. Neher, E. 1998. Vesicle pools and Ca²⁺ microdomains: new tools for understanding their roles in neurotransmitter release. *Neuron.* 20: 389–399.
12. Thurley, K., A. Skupin, R. Thul, and M. Falcke. 2012. Fundamental properties of Ca²⁺ signals. *Biochim. Biophys. Acta.* 1820: 1185–1194.
13. Dupont, G., M. Falcke, V. Kirk, and J. Sneyd. 2016. Models of Calcium Signalling. Springer International Publishing, Cham, Switzerland.
14. Roberts, W.M. 1993. Spatial calcium buffering in saccular hair cells. *Nature.* 363: 74–76.
15. Simon, S.M., and R.R. Llinas. 1985. Compartmentalization of the submembrane calcium activity during calcium influx and its significance in transmitter release. *Biophys. J.* 48: 485–498.
16. Fogelson, A.L., and R.S. Zucker. 1985. Presynaptic calcium diffusion from various arrays of single channels. Implications for transmitter release and synaptic facilitation. *Biophys. J.* 48: 1003–1017.

17. Chad, J.E., and R. Eckert. 1984. Calcium domains associated with individual channels can account for anomalous voltage relations of CA-dependent responses. *Biophys. J.* 45: 993–999.
18. Aharon, S., H. Parnas, and I. Parnas. 1994. The magnitude and significance of Ca²⁺ domains for release of neurotransmitter. *Bull. Math. Biol.* 56: 1095–1119.
19. Matthews, E.A., and D. Dietrich. 2015. Buffer mobility and the regulation of neuronal calcium domains. *Front. Cell. Neurosci.* 9: 48.
20. Neher, E. 1986. Concentration profiles of intracellular calcium in the presence of a diffusible chelator. *Exper. Brain Res.* 14: 80–96.
21. Neher, E. 1998. Usefulness and limitations of linear approximations to the understanding of Ca⁺⁺ signals. *Cell Calcium.* 24: 345–357.
22. Naraghi, M., and E. Neher. 1997. Linearized buffered Ca²⁺ diffusion in microdomains and its implications for calculation of [Ca²⁺] at the mouth of a calcium channel. *J. Neurosci.* 17: 6961–6973.
23. Pape, P. C., D.S. Jong, and W.K. Chandler. 1995. Calcium release and its voltage dependence in frog cut muscle fibers equilibrated with 20 mM EGTA. *J. Gen. Physiol.* 106: 259–336.
24. Stern, M.D. 1992. Buffering of calcium in the vicinity of a channel pore. *Cell Calcium.* 13:183–192.
25. Gillespie, D. 2020. Simulating diffusion from a cluster of point sources using propagation integrals. *Eur. Biophys. J.* 49:385–393.
26. Bauer, P.J. 2001. The local Ca concentration profile in the vicinity of a Ca channel. *Cell Biochem. Biophys.* 35: 49–61.
27. Wagner, J., and J. Keizer. 1994. Effects of rapid buffers on Ca²⁺ diffusion and Ca²⁺ oscillations. *Biophys. J.* 67: 447–456.
28. Smith, G.D., J. Wagner, and J. Keizer. 1996. Validity of the rapid buffering approximation near a point source of calcium ions. *Biophys. J.* 70: 2527–2539.
29. Smith, G.D. 1996. Analytical steady-state solution to the rapid buffering approximation near an open Ca²⁺ channel. *Biophys. J.* 71: 3064–3072.
30. Bertram, R., G.D. Smith, and A. Sherman. 1999. Modeling study of the effects of overlapping Ca²⁺ microdomains on neurotransmitter release. *Biophys. J.* 76: 735–750.
31. Bentele, K., and M. Falcke. 2007. Quasi-steady approximation for ion channel currents. *Biophys. J.* 93: 2597–2608.
32. Smith, G.D., L.X. Dai, R.M. Miura, and A. Sherman. 2001. Asymptotic analysis of buffered calcium diffusion near a point source. *SIAM J. Appl. Math.* 61: 1816–1838.
33. Duffy, A., J. Sneyd, and P.D. Dale. 1998. Traveling waves in buffered systems: applications to calcium waves. *SIAM J. Appl. Math.* 58: 1178–1192.

34. Coggins, M., and D. Zenisek. 2009. Evidence that exocytosis is driven by calcium entry through multiple calcium channels in goldfish retinal bipolar cells. *J. Neurophysiol.* 101: 2601–2619.
35. Nguyen, V., R. Mathias, and G.D. Smith. 2005. A stochastic automata network descriptor for Markov chain models of instantaneously coupled intracellular Ca²⁺ channels. *Bull. Math. Biol.* 67: 393–432.
36. Montefusco, F., and M.G. Pedersen. 2018. Explicit Theoretical Analysis of How the Rate of Exocytosis Depends on Local Control by Ca²⁺ Channels. *Hindawi Comput. Math. Methods Med.* 5721097:1-12.
37. Trommershauser, J., R. Schneggenburger, A. Zippelius, and E. Neher. 2003. Heterogeneous presynaptic release probabilities: functional relevance for short-term plasticity. *Biophys. J.* 84: 1563–1579.
38. Matveev, V. 2016. Padé Approximation of a Stationary Single-Channel Ca²⁺Nanodomain. *Biophys. J.* 111: 2062–2074.
39. Chen, Y., C. Muratov, and V. Matveev. 2020. Efficient approximations for stationary single-channel Ca²⁺ nanodomains across length scales. *Biophys. J.* 119:1239-1254.
40. Schwaller, B. 2009. The continuing disappearance of “pure” Ca²⁺ buffers. *Cell. Mol. Life Sci.* 66: 275–300.
41. Schwaller, B. 2014. Calretinin: from a “simple” Ca(2+) buffer to a multifunctional protein implicated in many biological processes. *Front. Neuroanat.* 8: 3.
42. Faas, G.C., B. Schwaller, J.L. Vergara, and I. Mody. 2007. Resolving the fast kinetics of cooperative binding: Ca²⁺ buffering by calretinin. *PLOS Biol.* 5: e311.
43. Chin, D., and A.R. Means. 2000. Calmodulin: a prototypical calcium sensor. *Trends Cell Biol.* 10: 322–328.
44. Raghuram, V., Y. Sharma, and M.R. Kreutz. 2012. Ca(2+) sensor proteins in dendritic spines: a race for Ca(2+). *Front. Mol. Neurosci.* 5: 61.
45. Saftenku, E.E. 2012. Effects of Calretinin on Ca(2+) Signals in Cerebellar Granule Cells: Implications of Cooperative Ca(2+) Binding. *Cerebellum.* 11: 102–120.
46. Faas, G.C., S. Raghavachari, J.E. Lisman, and I. Mody. 2011. Calmodulin as a direct detector of Ca²⁺ signals. *Nat. Neurosci.* 14: 301–304.
47. Kubota, Y., and M.N. Waxham. 2010. Lobe specific Ca²⁺-calmodulin nano-domain in neuronal spines: a single molecule level analysis. *PLOS Comput. Biol.* 6: e1000987.
48. Schwaller, B. 2020. Cytosolic Ca²⁺Buffers Are Inherently Ca²⁺Signal Modulators. *Cold Spring Harb. Perspect. Biol.* 12: a035543.
49. Matveev, V. 2018. Extension of Rapid Buffering Approximation to Ca²⁺ Buffers with Two Binding Sites. *Biophys. J.* 114: 1204–1215.
50. Falcke, M. 2003. Buffers and oscillations in intracellular Ca²⁺ dynamics. *Biophys. J.* 84: 28–41.

51. Falcke, M. 2003. On the role of stochastic channel behavior in intracellular Ca²⁺ dynamics. *Biophys. J.* 84: 42–56.
52. Ordyan, M., T. Bartol, M. Kennedy, P. Rangamani, and T. Sejnowski. 2020. Interactions between calmodulin and neurogranin govern the dynamics of CaMKII as a leaky integrator. *PLOS Comput. Biol.* 16: e1008015.
53. Matveev, V., A. Sherman, and R.S. Zucker. 2002. New and corrected simulations of synaptic facilitation. *Biophys. J.* 83: 1368–1373.
54. Muratov, C.B., P.V. Gordon, and S.Y. Shvartsman. 2011. Self-similar dynamics of morphogen gradients. *Phys. Rev. E.* 84: 041916.
55. Berezhkovskii, A.M., C. Sample, and S.Y. Shvartsman. 2011. Formation of morphogen gradients: Local accumulation time. *Phys. Rev. E.* 83: 051906.
56. Gordon, P.V., C.B. Muratov, and S.Y. Shvartsman. 2013. Local accumulation times for source, diffusion, and degradation models in two and three dimensions. *J. Chem. Phys.* 138: 104121.
57. Gordon, P.V., C. Sample, A.M. Berezhkovskii, C.B. Muratov, and S.Y. Shvartsman. 2011. Local kinetics of morphogen gradients. *PNAS USA.* 108: 6157–6162.
58. Gordon, P.V., and C.B. Muratov. 2015. Eventual Self-similarity of Solutions for the Diffusion Equation with Nonlinear Absorption and a Point Source. *SIAM J. Math. Analysis.* 47: 2903-2916.
59. Osipov, V.V. 1993. Multifunctional variational method for description of evolution and dynamics of dissipative structures in nonequilibrium systems. *Phys. Rev. E.* 48: 88–100.
60. Timofeeva, Y., and K.E. Volynski. 2015. Calmodulin as a major calcium buffer shaping vesicular release and short-term synaptic plasticity: facilitation through buffer dislocation. *Front. Cell. Neurosci.* 9: 239.
61. Keller, D.X., K.M. Franks, T.M.J. Bartol, and T.J. Sejnowski. 2008. Calmodulin activation by calcium transients in the postsynaptic density of dendritic spines. *PLOS One* 3: e2045.
62. Griffith, T., K. Tsaneva-Atanasova, and J.R. Mellor. 2016. Control of Ca²⁺ Influx and Calmodulin Activation by SK-Channels in Dendritic Spines. *PLOS Comput. Biol.* 12: e1004949.
63. Dick, I.E., M.R. Tadross, H. Liang, L.H. Tay, W. Yang, and D.T. Yue. 2008. A modular switch for spatial Ca²⁺ selectivity in the calmodulin regulation of CaV channels. *Nature.* 451: 830–834.
64. Helassa, N., X.H. Zhang, I. Conte, J. Scaringi, E. Esposito, J. Bradley, T. Carter, D. Ogden, M. Morad, and K. Torok. 2015. Fast-Response Calmodulin-Based Fluorescent Indicators Reveal Rapid Intracellular Calcium Dynamics. *Sci. Rep.* 5:15978.